Stochastic formation of quantum defects in carbon nanotubes

Chen Ma[a§], Christoph A. Schrage[a§], Juliana Gretz[a], Linda Sistemich[a], Lena Schnitzler[a], Han Li[c], Benjamin S. Flavel[c], Sebastian Kruss[a,b*].

[a] Department of Chemistry, Ruhr-University Bochum, Bochum, Germany

[b] Fraunhofer Institute for Microelectronic Circuits and Systems

[c] Institute of Nanotechnology, Karlsruhe Institute of Technology (KIT), Germany

ABSTRACT: Small perturbations in the structure of materials significantly affect their properties. One example are single wall carbon nanotubes (SWCNTs), which exhibit chirality-dependent near infrared (NIR) fluorescence. They can be modified with quantum defects through the reaction with diazonium salts and the number or distribution of these defects determine their photophysics. However, the presence of multiple chiralities in typical SWCNT samples complicates the identification of defect-related emission features. Here, we show that quantum defects do not affect aqueous two-phase extraction (ATPE) of different SWCNT chiralities into different phases, which pinpoints to low numbers of defects. For bulk samples the bandgap emission (E_{11}) of monochiral (6,5)-SWCNTs decreases and the defect related emission feature (E_{11}^*) increases with diazonium salt concentration and represents a proxy for the defect number. The high purity of monochiral samples from ATPE allows us to image NIR fluorescence contributions (E_{11} = 986 nm, and E_{11}^* = 1140 nm) on the single SWCNT level. Interestingly, we observe a stochastic (Poisson) distribution of quantum defects. SWCNTs have most-likely 1 to 3 defects (for low to high (bulk) quantum defect densities). Additionally, we verify this number by following single reaction events that appear as discrete steps in the temporal fluorescence traces. We thereby count single reactions via NIR imaging and demonstrate that stochasticity plays a crucial role for the optical properties of SWCNTs. These results show that there can be a large discrepancy between ensemble and single particle experiments/properties of nanomaterials.

The properties of solid-state materials depend on their structural and chemical purity. Recent advances in nanoparticle synthesis and preparation have shown that minor disturbances give rise to novel material characteristics. Techniques such as symmetry breaking and defect incorporation have been used to tailor hollow metal chalcogenide particles[1], engineer colloidal crystals with DNA[2,3] and create new emission features *via* nitrogen vacancy (NV) centers in nanodiamonds[4–6]. A material that is very susceptible to small changes in its structure and environment are carbon nanotubes (CNTs). They have rich optoelectronic and mechanical properties and broad potential for material science and biomedicine[7,8]. Among the different types of CNTs, single wall carbon nanotubes (SWCNTs) have become a multidisciplinary field[9–12], because of their intrinsic near-infrared (NIR) fluorescence (850-1700 nm)[13]. This property has been used to develop powerful biosensors for a range of analytes including small molecules, lipids, proteins, neurotransmitters, and sugars. Such sensors have been employed in complex biomedical applications such as fast neurotransmitter imaging[14–16], pathogen diagnostics[17,18], insulin detection[19], stress detection in plants[20–22], monitoring wound healing[23] or cancer marker detection[24–26].

A drawback of NIR fluorophores such as SWCNTs are their lower quantum yields. Interestingly, certain covalent modifications of the graphene lattice (sp^3 quantum defects) create highly emissive states that increase the overall quantum yield[27–30]. These quantum defects act as traps for mobile excitons from which red-shifted emission (E_{11}*) takes place[31]. Possible reactions to introduce defects include (a) ozone treatment[32], (b) reactions with aryldiazonium salts, which introduce sp^3 defects into the sp^2 lattice[28] and (c) [2π + 2π] photocycloaddition of enones[33], which all generate a red-shifted photoluminescence around 1130 nm for (6,5)-SWCNTs. In addition to the reactions mentioned above, there are other ways to introduce covalently functional groups such as π-preserving triazine conjugation but without new emission features[34]. Diazonium chemistry also offers to conjugate more complex entities such as biomolecules[35,36]. It is useful to directly attach e.g. nanobodies or grow peptide chains on the SWCNT lattice, which expands the toolbox for many applications such as sensing with quantum defects[37,38]. The concentration of diazonium salt affects the reaction and most likely the density of quantum defects. the ratio (E_{11}^*/E_{11}) between the quantum defect related

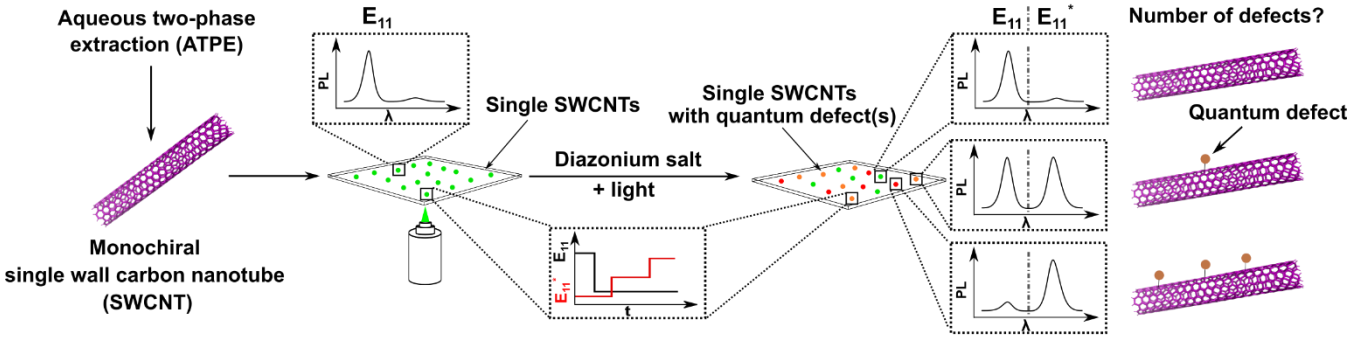

Figure 1. Counting of quantum defects in single SWCNTs. SWCNTs are sorted by aqueous two-phase extraction to yield pure (6,5)-SWCNTs with distinct E_{11} emission features and no spectral congestion in the near infrared (NIR). Quantum defects are introduced by the reaction with diazonium salts under light exposure and create a new red-shifted emission feature (E_{11}^*). Their distribution is then assessed by imaging the different spectral features either during the reaction itself or afterwards. This approach allows to quantify and count the number of defects and correlate it to the photophysical properties.

emission (E_{11}^*) and the bandgap emission (E_{11}) of SWCNTs is regarded as an approximate measure for defect density[39]. Wang et al. estimated in SWCNTs of maximum E_{11}^* photoluminescence about one defect per 20 nm length of (6,5)-SWCNTs[28]. Zaumseil et al. found defect densities ranging from around 5 (low) to 30 (high) defects per µm of SWCNT[40]. For (6,5)-SWCNTs, they recently measured sp^3 defects from low to medium densities at low temperatures (4.6 K), which equate to 4 μm^{-1} and 8 μm^{-1}, respectively, with an error of ±3 defects/µm[41]. Nevertheless, a complete understanding of how defects affect photophysics is still missing.

Even though there have been advances in synthesis of chirality-pure SWCNTs[42,43], commercially available SWCNTs typically contain different chiralities. Such mixtures of multiple SWCNT chiralities lead to overlapping and congested spectra. In contrast, purified SWCNTs show well-defined spectra and higher fluorescence emission[37,44]. These advantages make chirality-enriched or pure SWCNTs highly attractive[45] and are required to get well-defined SWCNT spectra e.g. for ratiometric or multiplexed sensing[17,44].

In the past years, the efficacy at which SWCNTs can be dispersed, enriched, and separated has significantly improved[46–53]. Purification methods include ion-exchange chromatography (IEX)[47,54], density-gradient ultracentrifugation (DGU)[55,56], selective extraction in organic solvents[57,58], gel chromatography[59–61] and aqueous two-phase extraction (ATPE)[62–66]. ATPE stands out among these methods, because it is relatively simple, provides a high reproducibility and up-scaling is straightforward. Zheng et al. reported an ATPE system which achieved complete sorting of DNA-SWCNTs[62]. Flavel and coworkers set up a simple pH sensitive ATPE process. In total 11 (n, m) species were isolated, not only including semiconducting but also metallic and non-armchair metallic species[63]. The partition mechanism of SWCNTs chiralities in ATPE is still not completely understood but one plausible explanation are differences in the chemical potential for different (n, m) species in these two phases[67]. Additionally, ATPE paired with surfactant exchange expands the potential for biological applications of SWCNTs[68].

Here, we combine ATPE of SWCNTs with quantum defect chemistry to quantify the number of quantum defects in single SWCNTs. For this purpose, we apply diazonium salt chemistry and elucidate the impact of defects on the overall ATPE process. Furthermore, we follow the reaction of monochiral (6,5)-SWCNTs on the single molecule and single SWCNT level by fluorescence microscopy. This allows us to count the number of quantum defects and compare the bulk and single particle picture.

To create SWCNTs with quantum defects (dSWCNTs), diazonium salt (4-nitrobenzoldiazonium tetrafluoroborate) was added to a sodium dodecyl benzenesulfonate (SDBS)-dispersed SWCNT solution and exposed to green light (550 nm, Figure 1). It is known that excessive amounts of sp^3 defects completely quench the NIR fluorescence of SWCNTs[69]. Therefore, the reaction conditions were optimized first. In the absence of 4-nitrobenzoldiazonium tetrafluoroborate, there is only one E_{11} emission peak at 976 nm (figure S1). With increasing concentration of diazonium salt, a new defect-related emission peak E_{11}^* appeared at 1120 nm. Its intensity increased with diazonium salt concentration,

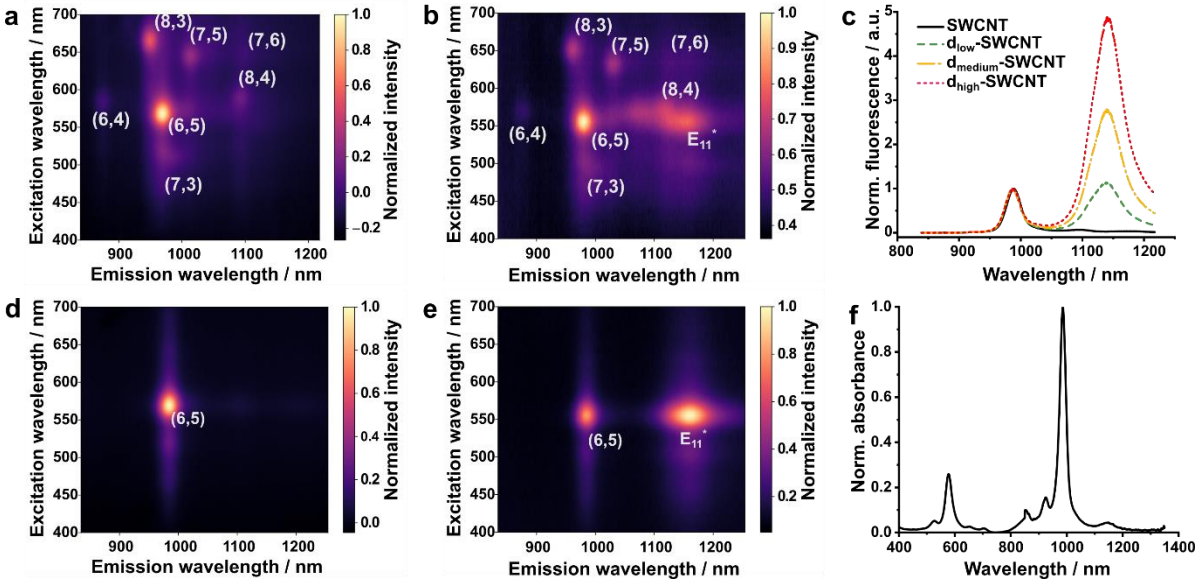

Figure 2. ATPE of SWCNTs with quantum defects. NIR 2D (a, d) fluorescence spectra of SWCNTs without defects and d_{low}-SWCNTs (b, e) with defects (reacted with 10 µM 4-nitrobenzoldiazonium tetrafluoroborate) before and after ATPE. (c) NIR 1D fluorescence spectra of pristine-, d_{low}-, d_{medium}-, d_{high}-SWCNTs after ATPE show that defects do not affect the ATPE process. The E_{11}^*/E_{11} ratio is considered as indicator of defect density. (f) Absorbance spectra of d_{low}-SWCNT after ATPE show mainly (6,5)-SWCNT related features.

while the intensity of the E_{11} peak decreased. With higher concentrations of the diazonium salt, the intensity of the E_{11}^* emission decreased until the overall fluorescence vanished. Reaction mixtures with 10 µM, 20 µM and 30 µM diazonium salt (here after referred to as d_{low}-, d_{medium}- and d_{high}-SWCNT) revealed the highest E_{11} and E_{11}^* intensities and were used for further experiments. In the absorbance spectra there was no new peak observed at around 1120 nm (Figure S2), which indicates a low density of quantum defects[28]. The success of the defect reaction can be followed by an increase of the E_{11}^* feature in both NIR 1D fluorescence (Figure S1a), Raman (Figure S1b) and 2D (Figure 2a, b) excitation-emission fluorescence spectra. Additionally, the 2D spectra revealed that the prepared pristine- and d_{low}-SWCNT solutions consisted not only of (6,5)-SWCNTs but also of other SWCNT chiralities. A reliable and easy ATPE approach[63] was used to enrich monochiral (6,5)-pristine-SWCNTs and (6,5)-d_{low}-SWCNTs and all steps were monitored by absorbance spectra of the respective top and bottom phases (Figure S3 and S4).

In the first step, HCl was added, which moved SWCNTs with larger diameter to the top phase 1 (T_1), and mainly (6,5), (6,4) chiralities remained in the bottom phase 1 (B_1). In the second step of ATPE, only (6,5) moved to the top phase 2 (T_2) and all other chiralities remained in the bottom phase 2 (B_2). In the last step, a separation of metallic and semiconducting SWCNTs was achieved and either (6,5)-pristine-SWCNTs or (6,5)-d_{low}-SWCNTs were collected in bottom phase 3 (B_3). During ATPE, monochiral d_{low}-SWCNTs could be extracted in the same way as monochiral pristine-SWCNTs, as can be seen by the presence of chirality-specific absorbance peaks in the spectra of each phase in each step (Figure S3 and S4). After ATPE, the absorbance and fluorescence spectra of SWCNTs showed mainly the E_{11} peak (around 986 nm) of pure (6,5)-SWCNTs (Figure S3f, 2c and 2d). Similarly, well-defined spectra were obtained for d_{low}-SWCNTs after ATPE. In the absorbance spectrum only the expected features such as the E_{11} and E_{22} peaks were present (Figure 2f). Well-defined E_{11} and E_{11}^* peaks were also observed in 1D (Figure 2c) and 2D (Figure 2e) excitation-emission fluorescence spectra. These results show that the ATPE protocol separates monochiral (6,5)-SWCNTs with quantum defects from a mixture of different chiralities.

Furthermore, the effect of diazonium salt concentration was explored. The E_{11}^*/E_{11} ratio increased in NIR 1D and 2D excitation-emission fluorescence spectra (Figure S1, 2b, S5a, and S5b), which indicates increased densities of quantum defects before ATPE. During ATPE, the top and bottom phase absorbance spectra from all steps are the same (Figure S4, S6, and S7), suggesting that the same chiralities were separated regardless of defect density. After ATPE, d_{medium}- and d_{high}-SWCNT spectra indicated pure (6,5)-dSWCNTs, comparable to d_{low}-SWCNTs (Figure 2c, 2e, S5c and S5d). The partition coefficient of pristine and SWCNTs with quantum defects into different phases was therefore identical. It can be explained by similar chemical potentials, which is supported e.g. by similar Zeta potentials of SWCNTs with different defect densities (Figure S8). All these findings pinpoint to a low number of defects per SWCNT.

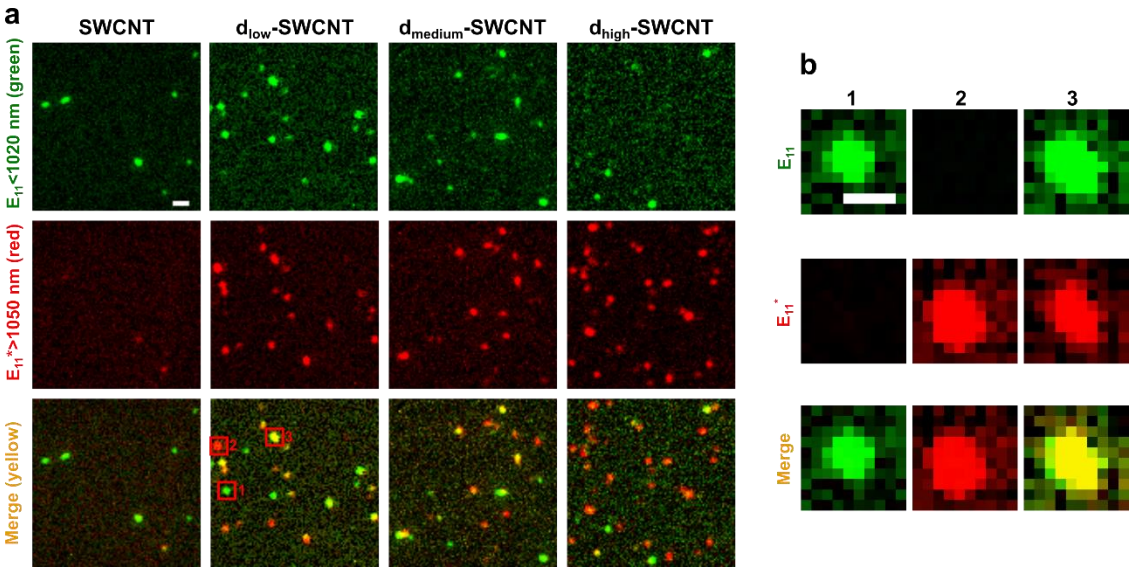

Figure 3. Single SWCNTs with quantum defects show spectral variation. (a) NIR fluorescence images of the E_{11} feature in green (shortpass, emission <1020 nm) and of the E_{11}^* feature in red (longpass, emission > 1050 nm) and the merged channels in yellow. The distribution indicates a huge heterogeneity in quantum defect numbers. Scale bar = 2 µm. (b) Magnified fluorescence image of single dSWCNTs 1-3 from (a). Particle 1 appears to show mainly E_{11} emission, indicating no quantum defects. Particle 2 shows mainly E_{11}^*, indicating that all excitons are trapped into defects states (high defect density). Particle 3 shows both spectral features. Scale bar is 1 µm.

Moreover, the yield (total SWCNT mass) of performing first the defect reaction and then ATPE for dSWCNTs (3.3 %) was similar to the one for ATPE of pristine SWCNTs followed by the defect reaction (around 2.7 %) and similar to literature values[70].

The different optical features of pristine and defect (6,5)-SWCNTs (after ATPE) allow us to observe defects on the single SWCNT level (Figure 3). For this purpose, NIR fluorescence images were taken in the spectral range of the E_{11} emission (< 1020 nm) and of the E_{11}* emission (>1050 nm). This spectral separation was only possible because of the high purity of the samples after ATPE without other chiralities of SWCNTs that could overlap with these emission features (figure 2). Interestingly, we observed a large heterogeneity on the single SWCNT level. Some SWCNTs showed only E_{11} signals (figure 3b, SWCNT 1), some only E_{11}^*

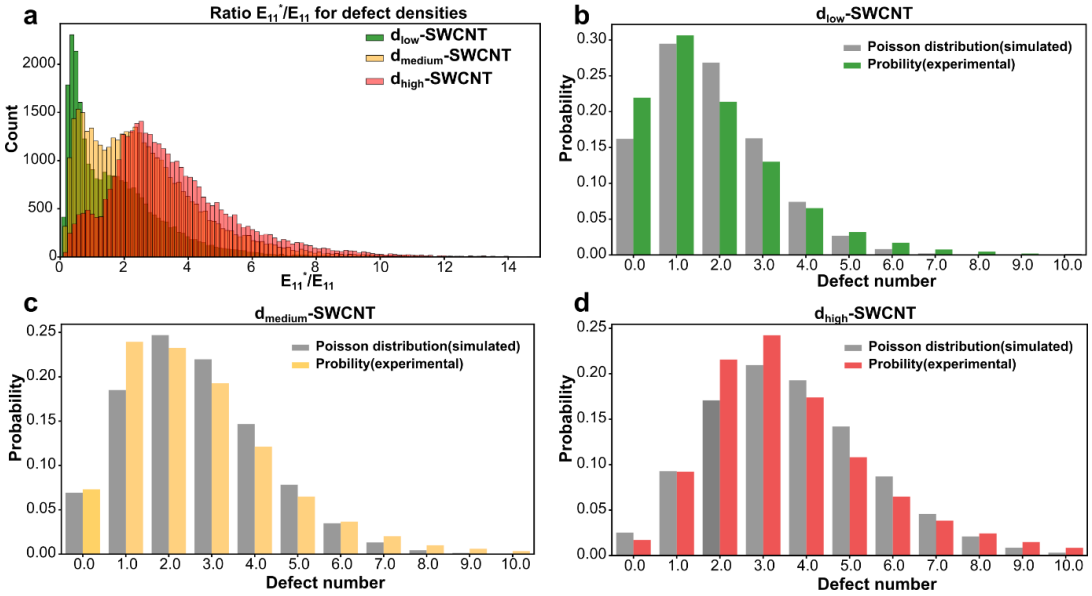

Figure 4. Number of quantum defects follows a Poisson distribution. (a) E_{11}^*/E_{11} ratio (proxy for defect density) of d_{low}-, d_{medium}- and d_{high}- single SWCNTs. (b-d) Probability for finding a certain defect number (proportional to E_{11}^*/E_{11} ratio) in single SWCNTs and fitted Poisson distributions of (b) d_{low}-SWCNT (n=26708), (c) d_{medium}-SWCNT (n=39070), and (d) d_{high}-SWCNT (n=35302). n is the number of single SWCNTs that were evaluated. R^2 fit values are 0.968 (b), 0.956 (c) and 0.938 (d).

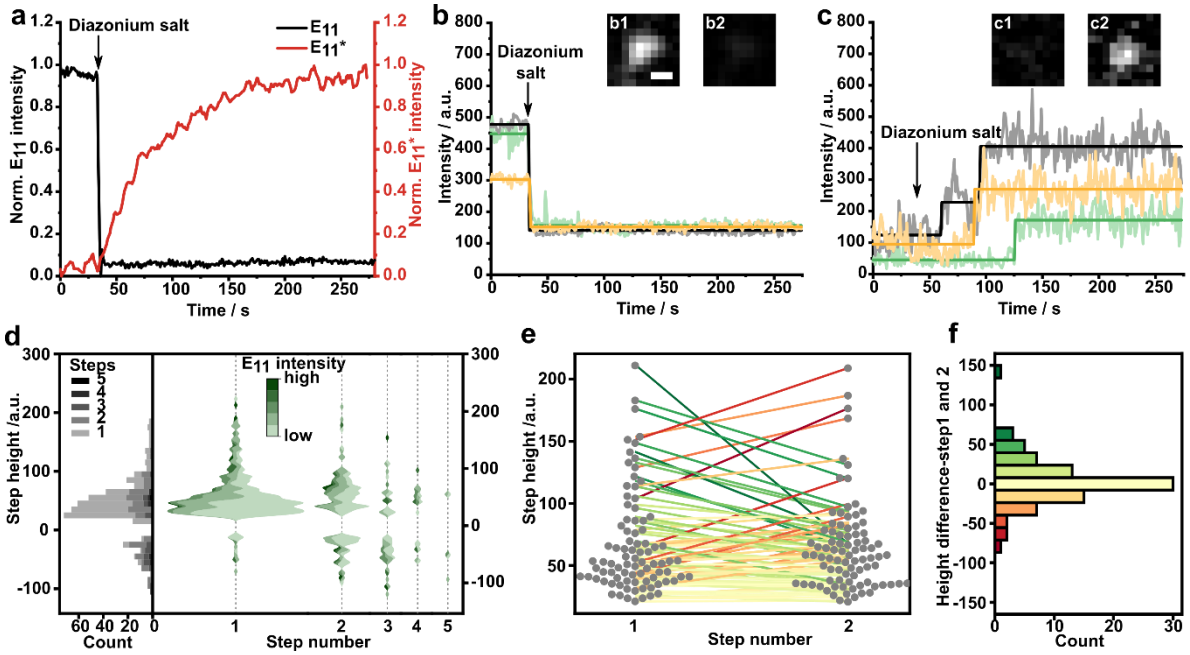

Figure 5. Observation and counting the formation of single quantum defects. (a) Overall fluorescence trace (E_{11} and E_{11}^* signal) of a population of SWCNTs (n=458) during defect reaction. (b) Fluorescence trace and fitted steps of single SWCNTs (E_{11} signal) during defect reaction. Image (b1, b2) of a single SWCNT before and after addition of diazonium salt (yellow trace). (c) Fluorescence trace and fitted steps of single SWCNTs (E_{11}^*). Image (c1, c2) of a single SWCNT before and after the reaction with a diazonium salt (yellow trace in c). Scale bar is 1 µm. (d) Height of each step as histogram (grey scale indicates step number) and height as function of step number (color code indicates pre-reaction E_{11} emission intensity, occurrence is proportional to area). (e) Comparison between all positive consecutive reaction steps 1 and 2. (f) Height difference from all pairs in (e) and their occurrence show that for the first two quantum defects the absolute changes in intensity are similar. This makes sense in the limit of small defect numbers when they are most likely independent exciton traps.

signals (figure 3b, SWCNT 2) and some both signals (figure 3b, SWCNT 3). On the other hand, by comparing the fluorescence intensities of E_{11} and E_{11}^* on a single SWCNT level, the different defect densities of dSWCNTs became qualitatively and also quantitatively visible. This way the E_{11}^*/E_{11} ratio of thousands of particles could be measured (figure 4) and as expected, the mean ratio shifted to higher values with the increased defect densities (figure 4a). The ratio of E_{11}^*/E_{11} was interpreted to change linearly with the number of defects and the probability of defect numbers on one SWCNT was calculated with a Poisson probability mass function:

$$P_{(X=k)} = \frac{\lambda^k e^{-\lambda}}{k!}$$

in which:

$$\lambda = \langle X \rangle = \langle \frac{E_{11}^*}{E_{11}} \rangle \sim \langle n_{defect} \rangle$$

λ is the mean ratio of $E_{11}^*$and E_{11} (~mean number of defects) and k is the discrete defect number. Even though the distributions of each defect state (Figure 4a) are diverse from one another, they are not discrete. This is to be expected as the length distribution of the SWCNTs is also heterogeneous, as well as their quantum yield[65]. To compare the experimental with the discrete Poisson distributions, it was necessary to classify the experimental ratios to obtain discrete values. For this reason, the non-defect state had to be estimated from the ratios of SWCNTs whose E_{11}^* intensity was equal to or lower than the background noise (Figure S12). A ratio of 0.5 appeared appropriate, given the bulk of SWCNTs in this category fell below this range and SWCNTs with ratios greater than 0.5 were predicted to be either extremely short or to have a relatively poor quantum yield. Therefore, E_{11}^*/E_{11} ratios were summed up uniformly around each natural number with a spread of one (every ratio between 0.5 and 1.5 counts towards the discrete ratio of 1). The discrete experimental distribution was fitted very well by the Poisson distribution (Figure 4b, c, d). Given the length of (6,5)-SWCNTs after ATPE of similar samples from our previous work[44] (~ 1000 nm), the mean defect densities are calculated as 1.7 to 3.5 µm^{-1} (1 to 3 defects per SWCNT, d_{low}- to d_{high}-SWCNTs).

To further explore and understand the influence of diazonium salts on single SWCNTs, the defect reaction was monitored in real-time in both E_{11} and E_{11}^* channels (Figure S9, Supplementary Video S1 and S2). Interestingly, the two spectral contributions were not synchronous as the overall fluorescence intensity (Figure 5a).

The E_{11} brightness decreased directly with the addition of the diazonium salt, while the E_{11}^* emission slowly increased over time (10 s – 200 s). This pattern could be explained by a two-step mechanism[71–74]: 1) diazonium salt adsorbs on the SWCNT surface and directly quenches the E_{11} emission. 2) The diazonium salt reacts with the SWCNT, which generates sp^3 defects and increases E_{11}^* emission. The total (bulk) fluorescence can be calculated from single SWCNT data by summing up the contributions of individual SWCNTs for the E_{11} and E_{11}^* channel:

$$I_{(t)}^{bulk} = \sum_{i=1}^{n} I_{(i,t)}$$

Here, I is the intensity of the respective spectral feature (E_{11} or E_{11}^*). To examine single defect reactions on single particles the changes of brightness of single SWCNTs were tracked. For the E_{11} channel, E_{11} intensities of single SWCNTs directly decreased (figure 5b), which resembles the bulk picture (figure 5a). Afterwards E_{11} intensities did not change anymore. On the contrary, the E_{11}^* intensities of single SWCNTs showed a diverse behavior (Figure 5c). These observations are in good agreement with the stochasticity of quantum defects in SWCNTs.

The E_{11}^* intensity of some SWCNTs directly increased stepwise after the diazonium salt was added, while others stayed unchanged for some seconds and then increased once or multiple times. These steps suggest that they represent the formation of one sp^3 defect similar to other reactions on SWCNTs[69,75,76]. With the help of a step-fitting algorithm (see materials and methods), the defect reactions of n= 458 single SWCNTs were analyzed (Figure S10a). 42% of SWCNTs did not have any defect, around 36% of SWCNTs had one defect, 18% of SWCNTs had two defects, and 4% of SWCNTs had three or four defects. The percentage of defects on SWCNT was a little bit lower but similar to d_{low}-SWCNT (Figure 4b, figure 2c) and also in agreement with the ensemble spectrum from the surface (Figure S9). These differences can be attributed to the different reaction conditions. For monitoring the reaction live (figure 5) the excitation light was a laser, which probably affected the effective diazonium salt concentration. The different individual onset times of the E_{11}^* increase (figure 5c) cause the smooth (bulk) fluorescence increase (figure 5a) of all SWCNTs. When summed up, all single SWCNT step heights and quantities overlap with the bulk E_{11}^* intensity change (figure S10b).

To further evaluate the distribution of steps, we examined the step-height of consecutive steps (figure 5d). With higher E_{11} starting intensities, the step heights (area inside the wave for each individual intensity relative to the others) increased slightly, and consecutive steps had comparable heights (Figure 5e and 5f, figure S11). This finding makes sense considering the typical length of our SWCNTs (around 1000 nm) and the typical diffusion length (100 nm) of excitons[77]. In the limit of low defect numbers, they can be considered independent and exciton trapping is independent. This interconnection is also relevant for the question how short a SWCNT with a single quantum defect could be for maximal quantum yield[78].

Given that we did not observe many multistep reactions the statistics were not unambiguous enough to perform the step height comparison for step numbers of two or more. We also observed 'negative' (figure 5d) steps, which increased with step number. We attribute them to noise from charges on the glass surface, organic corona dynamics and noise of the NIR camera.

In conclusion, we have quantified the number of sp^3 quantum defects in (6,5)-SWCNTs using fluorescence imaging and spectroscopy. We established a linear relationship between the different optical features and the sp^3 defect number. Most importantly, we found that quantum defects in SWCNTs follow a Poisson function with very low numbers (n=0-3). Moreover, we could follow and also count the incorporation of quantum defects live in the microscope on the single nanoparticle and single molecule level. This work provides deep insights into how tiny perturbations (single quantum defects) at the level of individual units in a carbon lattice fundamentally alter the optoelectronic properties. It paves the way for precise tuning and understanding of material properties using quantum defects and color centers. Such developments are the basis for advances in photonics such as single photon quantum protocols as well as imaging and (bio)sensing.

MATERIALS AND METHODS

Materials

If not otherwise specified, materials were received from Sigma-Aldrich.

Preparation of carbon nanotubes

CoMoCat (6,5)-chirality enriched single-walled carbon nanotubes (SWCNTs) were dispersed with sodium dodecylbenzenesulfonate (SDBS). In brief, 500 µL 2 mg/mL SWCNTs/water suspension was added to 500 µL 2 % (m/v) SDBS solution, tip sonicated for 20 min with 40 % amplitude at 4 °C (Fisher ScientificTM Model 120 Sonic Dismembrator, 48 W) and centrifuged for 30 min at 21000 g. Then the supernatant was collected, transferred to a fresh tube and centrifuged again for 30 min at 21000 g. This step was repeated one more time, the supernatant was collected and the SWCNT/SDBS dispersion stored at 4 °C for the defect reaction.

Defect reaction

The defect reaction was performed according to a previously developed protocol[31]. Firstly, the reaction conditions between diazonium salt and SWCNTs were tested in a Lumidox 96-well green LED array (λ = 550 nm). 180 µL SWCNT solution (50 nM) were mixed with 20 µL of 4-nitrobenzoldiazonium tetrafluoroborate of different concentrations (from 1 µM to 100 µM) in a 96-well plate and illuminated with the LED array for 15 min at 25 mA. Afterwards the reaction was verified with NIR-fluorescence spectroscopy (see spectroscopy section).

For a preparative defect reaction followed by ATPE, the volume of the reaction was scaled up to a final volume of 45 ml with total concentrations of 50 nM SWCNTs and 10-30 µM diazonium salt according to the protocol [31]. In brief, a Falcon tube containing a large volume of SWCNTs/SDBS solution was put inside the LED-photoreactor and then the diazonium salt was added to yield the desired concentration. The sample was irradiated at full power for 15 min under stirring and a large amount of dSWCNTs was acquired after removing the diazonium salt by molecular weight cut-off filtration.

Later an organic solvent assisted surfactant exchange experiment was performed to receive DOC dispersed SWCNTs for ATPE[79]. In detail, a certain volume of acetonitrile was mixed with SDBS-dSWCNTs solution to precipitate SWCNTs, then it was washed with water to remove residual SDBS. Finally, the SWCNTs were redispersed with 1% DOC solution,

tip sonicated for 5 min and centrifuged at 21000 g. The DOC-dSWCNT solution was obtained by collecting the supernatant.

Aqueous two-phase extraction (ATPE)

The separation was performed following the protocol by Li et al[56]. DOC-SWCNTs were with PEG (MW 6000 Da, 8% m/m), dextran (MW 70000 Da, 4% m/m) and SDS (0.5% m/v). Then, the SWCNT chiralities in the two phases could be adjusted by adding HCl. After three steps, monochiral (6,5)-SWCNTs (without or with defect) could be collected in the bottom phase (B3). Next, the solution was dialysed (300 kDa dialysis bag, Spectra/Por, Spectrum Laboratories Inc.) against 1% DOC solution to remove Dextran and obtain stable solutions.

Spectroscopy of SWCNTs

Absorbance spectra were measured with a JASCO V-670 device from 400 to 1350 nm in 0.2 nm steps in a 10 mm path length polystyrol/polystyrene cuvette (SARSTEDT, Germany). 1D-NIR fluorescence spectra were obtained with a Shamrock 193i spectrometer (Andor Technology Ltd., Belfast, Northern Ireland) connected to an IX73 Microscope (Olympus, Tokyo, Japan). Excitation was performed with a gem 561 laser (Laser Quantum, Stockport, UK). 2D excitation-emission spectra were collected with a Monochromator MSH150 instrument, equipped with a LSE341 light source (LOT-Quantum Design GmbH, Darmstadt, Germany) as the excitation source in the setup described above.

The concentration of SWCNTs was calculated with the equation developed by Weisman´s and Hertel´s group[80,81]. It is based on the full width at half maximum (FWHM) and absorbance maximum.

Fluorescence microscopy

First, a purified dSWCNT solution (0.02 nM) was immobilized on a glass surface for 1 to 2 hours to image single SWCNTs. The residual SWCNT solution was removed, and the surface washed with water 2-3 times to remove unbound SWCNTs. For imaging, an Olympus IX73 microscope with 100x objective lens (UPLSAPO100XS, Olympus, Tokyo, Japan) was employed. The samples were excited at 561 nm with a 100 mW laser (Cobolt Jive™ laser, Cobolt AB, Solna, Sweden). The images were acquired with an Andor Zyla 5.5 sCMOS camera (Andor Technology Ltd., Belfast, UK) at 1s exposure time. In this case, a short pass filter (AHF analysentechnik AG, 935/170 BrightLine HC) which wavelength range is from 850 nm to 1020 nm was employed to block E_{11}^* intensity. While for the signal of E_{11}^*, a long pass filter (Thorlabs, FELH1050) was used to exclude the signal below 1050 nm.

For the two-channel imaging, the microscope, objective and laser were the same as stated before. The images were captured with a VIS camera (PCO edge 4.2 bi, Kelheim, Germany) and a XEVA (Xenics, Leuven Belgium) NIR optimized InGaAs camera. And a dichroic mirror (AHF analysentechnik AG, HC R1064) was inserted to split the signal into two cameras. In this case, the VIS camera only captured the signal below 1064 nm corresponding to the E_{11} wavelength range, while the E_{11}^* intensity was observed with the NIR camera, so the E_{11} and E_{11}^* signal SWCNT could be seen at the same time.

Based on the two-channel set up, an on-sight defect reaction was performed. Around 0.25 nM purified (6,5)-SWCNT solution (1% SDBS) was incubated on a glass bottom petri dish for 2 hours to yield single SWCNTs on glass. Washing was performed as previously described. 200 µL 1% SDBS was added ontop of the immobilized SWCNTs, two camera recording was started with the laser on and 2 µL diazonium salt was added to monitor the intensity change of single SWCNTs over time in both channels.

Poisson simulation

The simulation was written in Python to check if the ratio between the E_{11}^* and E_{11} intensities of defect (6,5)-SWCNTs is discrete. To achieve this, the code was written to identify and track the particles in two different fluorescence channels (E_{11} and E_{11}^*). All particle coordinates were identified with a python toolkit named trackpy (minmass = 2, everything else on default). As the coordinates refer to the middle point of SWCNTs, a 7x7 pixel section was selected to capture the whole SWCNT signal. Overlaying a 7x7 gaussian mask helped to exclude the background. So, for every SWCNT, its 7x7 intensity array was multiplied with the gaussian mask to calculate the sum of the array. This value was extracted for every SWCNT coordinate. The intensity of all particles was calculated, so that the ratio of E_{11}^*/E_{11} for SWCNTs with different defect densities was calculated. The defect number (k) in the Poisson probability mass function was set between 1 and 10, as previous studies have shown only a low number of defects per nanotube[34].

Step fitting

For every video, all particle coordinates and intensities were identified the same way as for the Poisson simulation. These values were extracted for every SWCNT coordinate and every timeframe, resulting in multiple intensity vs time plots for multiple SWCNT signals.

To fit steps into these intensity vs time plots, the concept of "moving average absolute deviation (MAD)" was used. It calculates the absolute difference between a datapoint and the mean of a set of following datapoints (n=30), this gives insights about step movement in the data. As steps were translated to peaks, and to find the peaks automatically, the scipy toolkit "signal.find_peaks" was used. Next, the step height was filtered, to ensure only relevant steps were considered. For this, a threshold was set to a minimal step height of 75% the RMSF (root mean square fluctuation) of the dataset. This procedure resulted in time stems for steps. Finishing, the mean value in between all timesteps was calculated[75,82].

ASSOCIATED CONTENT

Supporting Information. Additional absorbance and fluorescence spectra, single particle behaviors analysis.

AUTHOR INFORMATION

Corresponding Author

* Sebastian Kruss, Email: sebastian.kruss@rub.de.

Author Contributions

§C. M. and A. S. contributed equally to this paper.

Notes

The authors declare no competing financial interest.

ACKNOWLEDGMENT

Funded by the Deutsche Forschungsgemeinschaft (DFG, German Research Foundation) under Germany´s Excellence Strategy – EXC 2033 – 390677874 – RESOLV. This work is supported by the „Center for Solvation Science ZEMOS funded by the German Federal Ministry of Education and Research BMBF and by the Ministry of Culture and Research of Nord Rhine-Westphalia. We thank the DFG for funding within the Heisenberg program (S.K. & B.S.F). C.M. is financially supported by the China Scholarship Council. B.S.F. and H.L. gratefully acknowledge support from the DFG under grant numbers FL 834/5-1, FL 834/7-1, FL 834/9-1 and FL 834/12-1.

REFERENCES

(1) Shen, B.; Huang, L.; Shen, J.; Hu, X.; Zhong, P.; Zheng, C. Y.; Wolverton, C.; Mirkin, C. A. Morphology Engineering in Multicomponent Hollow Metal Chalcogenide Nanoparticles. *ACS Nano* **2023**. https://doi.org/10.1021/acsnano.2c10667.

(2) Laramy, C. R.; O'Brien, M. N.; Mirkin, C. A. Crystal Engineering with DNA. *Nat Rev Mater* **2019**, *4* (3), 201–224. https://doi.org/10.1038/s41578-019-0087-2.

(3) Distler, M. E.; Landy, K. M.; Gibson, K. J.; Lee, B.; Weigand, S.; Mirkin, C. A. Symmetry-Breaking Dendrimer Synthons in Colloidal Crystal Engineering with DNA. *J Am Chem Soc* **2023**, *145* (2), 841–850. https://doi.org/10.1021/jacs.2c08599.

(4) Radtke, M.; Bernardi, E.; Slablab, A.; Nelz, R.; Neu, E. Nanoscale Sensing Based on Nitrogen Vacancy Centers in Single Crystal Diamond and Nanodiamonds: Achievements and Challenges. *Nano Futures* **2019**, *3* (4), 042004. https://doi.org/10.1088/2399-1984/ab5f9b.

(5) Schirhagl, R.; Chang, K.; Loretz, M.; Degen, C. L. Nitrogen-Vacancy Centers in Diamond: Nanoscale Sensors for Physics and Biology. *Annu Rev Phys Chem* **2014**, *65* (1), 83–105. https://doi.org/10.1146/annurev-physchem-040513-103659.

(6) Balasubramanian, G.; Chan, I. Y.; Kolesov, R.; Al-Hmoud, M.; Tisler, J.; Shin, C.; Kim, C.; Wojcik, A.; Hemmer, P. R.; Krueger, A.; Hanke, T.; Leitenstorfer, A.; Bratschitsch, R.; Jelezko, F.; Wrachtrup, J. Nanoscale Imaging Magnetometry with Diamond Spins under Ambient Conditions. *Nature* **2008**, *455* (7213), 648–651. https://doi.org/10.1038/nature07278.

(7) Ackermann, J.; Metternich, J. T.; Herbertz, S.; Kruss, S. Biosensing with Fluorescent Carbon Nanotubes. *Angewandte Chemie International Edition* **2022**, *61* (18). https://doi.org/10.1002/anie.202112372.

(8) Hong, G.; Diao, S.; Antaris, A. L.; Dai, H. Carbon Nanomaterials for Biological Imaging and Nanomedicinal Therapy. *Chem Rev* **2015**, *115* (19), 10816–10906. https://doi.org/10.1021/acs.chemrev.5b00008.

(9) Antonucci, A.; Kupis-Rozmysłowicz, J.; Boghossian, A. A. Noncovalent Protein and Peptide Functionalization of Single-Walled Carbon Nanotubes for Biodelivery and Optical Sensing Applications. *ACS Appl Mater Interfaces* **2017**, *9* (13), 11321–11331. https://doi.org/10.1021/acsami.7b00810.

(10) Moser, M. L.; Li, G.; Chen, M.; Bekyarova, E.; Itkis, M. E.; Haddon, R. C. Fast Electrochromic Device Based on Single-Walled Carbon Nanotube Thin Films. *Nano Lett* **2016**, *16* (9), 5386–5393. https://doi.org/10.1021/acs.nanolett.6b01564.

(11) Hendler-Neumark, A.; Bisker, G. Fluorescent Single-Walled Carbon Nanotubes for Protein Detection. *Sensors* **2019**, *19* (24), 5403. https://doi.org/10.3390/s19245403.

(12) Antonucci, A.; Reggente, M.; Roullier, C.; Gillen, A. J.; Schuergers, N.; Zubkovs, V.; Lambert, B. P.; Mouhib, M.; Carata, E.; Dini, L.; Boghossian, A. A. Carbon Nanotube Uptake in Cyanobacteria for Near-Infrared Imaging and Enhanced Bioelectricity Generation in Living Photovoltaics. *Nat Nanotechnol* **2022**, *17* (10), 1111–1119. https://doi.org/10.1038/s41565-022-01198-x.

(13) O'Connell, M. J.; Bachilo, S. M.; Huffman, C. B.; Moore, V. C.; Strano, M. S.; Haroz, E. H.; Rialon, K. L.; Boul, P. J.; Noon, W. H.; Kittrell, C.; Ma, J.; Hauge, R. H.; Weisman, R. B.; Smalley, R. E. Band Gap Fluorescence from Individual Single-Walled Carbon Nanotubes. *Science* **2002**, *297* (5581), 593–596. https://doi.org/10.1126/science.1072631.

(14) Kruss, S.; Salem, D. P.; Vuković, L.; Lima, B.; vander Ende, E.; Boyden, E. S.; Strano, M. S. High-Resolution Imaging of Cellular Dopamine Efflux Using a Fluorescent Nanosensor Array. *Proceedings of the National Academy of Sciences* **2017**, *114* (8), 1789–1794. https://doi.org/10.1073/pnas.1613541114.

(15) Elizarova, S.; Chouaib, A. A.; Shaib, A.; Hill, B.; Mann, F.; Brose, N.; Kruss, S.; Daniel, J. A. A Fluorescent Nanosensor Paint Detects Dopamine Release at Axonal Varicosities with High Spatiotemporal Resolution. *Proceedings of the National Academy of Sciences* **2022**, *119* (22). https://doi.org/10.1073/pnas.2202842119.

(16) Ackermann, J.; Stegemann, J.; Smola, T.; Reger, E.; Jung, S.; Schmitz, A.; Herbertz, S.; Erpenbeck, L.; Seidl, K.; Kruss, S. High Sensitivity Near-Infrared Imaging of Fluorescent Nanosensors. *Small* **2023**, 2206856. https://doi.org/10.1002/smll.202206856.

(17) Nißler, R.; Bader, O.; Dohmen, M.; Walter, S. G.; Noll, C.; Selvaggio, G.; Groß, U.; Kruss, S. Remote near Infrared Identification of Pathogens with Multiplexed

Nanosensors. *Nat Commun* **2020**, *11* (1), 5995. https://doi.org/10.1038/s41467-020-19718-5.

(18) Agarwal, S.; Kallmyer, N. E.; Vang, D. X.; Ramirez, A. v.; Islam, M. M.; Hillier, A. C.; Halverson, L. J.; Reuel, N. F. Single-Walled Carbon Nanotube Probes for the Characterization of Biofilm-Degrading Enzymes Demonstrated against *Pseudomonas Aeruginosa* Extracellular Matrices. *Anal Chem* **2022**, *94* (2), 856–865. https://doi.org/10.1021/acs.analchem.1c03633.

(19) Ehrlich, R.; Hendler-Neumark, A.; Wulf, V.; Amir, D.; Bisker, G. Optical Nanosensors for Real-Time Feedback on Insulin Secretion by B-Cells. *Small* **2021**, *17* (30), 2101660. https://doi.org/10.1002/smll.202101660.

(20) Nißler, R.; Müller, A. T.; Dohrman, F.; Kurth, L.; Li, H.; Cosio, E. G.; Flavel, B. S.; Giraldo, J. P.; Mithöfer, A.; Kruss, S. Detection and Imaging of the Plant Pathogen Response by Near-Infrared Fluorescent Polyphenol Sensors. *Angewandte Chemie International Edition* **2022**, *61* (2). https://doi.org/10.1002/anie.202108373.

(21) Giraldo, J. P.; Wu, H.; Newkirk, G. M.; Kruss, S. Nanobiotechnology Approaches for Engineering Smart Plant Sensors. *Nat Nanotechnol* **2019**, *14* (6), 541–553. https://doi.org/10.1038/s41565-019-0470-6.

(22) Wu, H.; Nißler, R.; Morris, V.; Herrmann, N.; Hu, P.; Jeon, S.-J.; Kruss, S.; Giraldo, J. P. Monitoring Plant Health with Near-Infrared Fluorescent H_2O_2 Nanosensors. *Nano Lett* **2020**, *20* (4), 2432–2442. https://doi.org/10.1021/acs.nanolett.9b05159.

(23) Safaee, M. M.; Gravely, M.; Roxbury, D. A Wearable Optical Microfibrous Biomaterial with Encapsulated Nanosensors Enables Wireless Monitoring of Oxidative Stress. *Adv Funct Mater* **2021**, *31* (13), 2006254. https://doi.org/10.1002/adfm.202006254.

(24) Yaari, Z.; Yang, Y.; Apfelbaum, E.; Cupo, C.; Settle, A. H.; Cullen, Q.; Cai, W.; Roche, K. L.; Levine, D. A.; Fleisher, M.; Ramanathan, L.; Zheng, M.; Jagota, A.; Heller, D. A. A Perception-Based Nanosensor Platform to Detect Cancer Biomarkers. *Sci Adv* **2021**, *7* (47). https://doi.org/10.1126/sciadv.abj0852.

(25) Budhathoki-Uprety, J.; Shah, J.; Korsen, J. A.; Wayne, A. E.; Galassi, T. v.; Cohen, J. R.; Harvey, J. D.; Jena, P. v.; Ramanathan, L. v.; Jaimes, E. A.; Heller, D. A. Synthetic Molecular Recognition Nanosensor Paint for Microalbuminuria. *Nat Commun* **2019**, *10* (1), 3605. https://doi.org/10.1038/s41467-019-11583-1.

(26) Williams, R. M.; Lee, C.; Galassi, T. V.; Harvey, J. D.; Leicher, R.; Sirenko, M.; Dorso, M. A.; Shah, J.; Olvera, N.; Dao, F.; Levine, D. A.; Heller, D. A. Noninvasive Ovarian Cancer Biomarker Detection via an Optical Nanosensor Implant. *Sci Adv* **2018**, *4* (4). https://doi.org/10.1126/sciadv.aaq1090.

(27) Brozena, A. H.; Kim, M.; Powell, L. R.; Wang, Y. Controlling the Optical Properties of Carbon Nanotubes with Organic Colour-Centre Quantum Defects. *Nat Rev Chem* **2019**, *3* (6), 375–392. https://doi.org/10.1038/s41570-019-0103-5.

(28) Piao, Y.; Meany, B.; Powell, L. R.; Valley, N.; Kwon, H.; Schatz, G. C.; Wang, Y. Brightening of Carbon Nanotube Photoluminescence through the Incorporation of Sp3 Defects. *Nat Chem* **2013**, *5* (10), 840–845. https://doi.org/10.1038/nchem.1711.

(29) Miyauchi, Y.; Iwamura, M.; Mouri, S.; Kawazoe, T.; Ohtsu, M.; Matsuda, K. Brightening of Excitons in Carbon Nanotubes on Dimensionality Modification. *Nat Photonics* **2013**, *7* (9), 715–719. https://doi.org/10.1038/nphoton.2013.179.

(30) Janas, D. Perfectly Imperfect: A Review of Chemical Tools for Exciton Engineering in Single-Walled Carbon Nanotubes. *Mater Horiz* **2020**, *7* (11), 2860–2881. https://doi.org/10.1039/D0MH00845A.

(31) Zaumseil, J. Luminescent Defects in Single-Walled Carbon Nanotubes for Applications. *Adv Opt Mater* **2022**, *10* (2), 2101576. https://doi.org/10.1002/adom.202101576.

(32) Ghosh, S.; Bachilo, S. M.; Simonette, R. A.; Beckingham, K. M.; Weisman, R. B. Oxygen Doping Modifies Near-Infrared Band Gaps in Fluorescent Single-Walled Carbon Nanotubes. *Science (1979)* **2010**, *330* (6011), 1656–1659. https://doi.org/10.1126/science.1196382.

(33) He, X.; Kevlishvili, I.; Murcek, K.; Liu, P.; Star, A. [2π + 2π] Photocycloaddition of Enones to Single-Walled Carbon Nanotubes Creates Fluorescent Quantum Defects. *ACS Nano* **2021**, *15* (3), 4833–4844. https://doi.org/10.1021/acsnano.0c09583.

(34) Setaro, A.; Adeli, M.; Glaeske, M.; Przyrembel, D.; Bisswanger, T.; Gordeev, G.; Maschietto, F.; Faghani, A.; Paulus, B.; Weinelt, M.; Arenal, R.; Haag, R.; Reich, S. Preserving π-Conjugation in Covalently Functionalized Carbon Nanotubes for Optoelectronic Applications. *Nat Commun* **2017**, *8* (1), 14281. https://doi.org/10.1038/ncomms14281.

(35) Mann, F. A.; Herrmann, N.; Opazo, F.; Kruss, S. Quantum Defects as a Toolbox for the Covalent Functionalization of Carbon Nanotubes with Peptides and Proteins. *Angewandte Chemie International Edition* **2020**, *59* (40), 17732–17738. https://doi.org/10.1002/anie.202003825.

(36) Mann, F. A.; Galonska, P.; Herrmann, N.; Kruss, S. Quantum Defects as Versatile Anchors for Carbon Nanotube Functionalization. *Nat Protoc* **2022**, *17*

(3), 727–747. https://doi.org/10.1038/s41596-021-00663-6.

(37) Spreinat, A.; Dohmen, M. M.; Lüttgens, J.; Herrmann, N.; Klepzig, L. F.; Nißler, R.; Weber, S.; Mann, F. A.; Lauth, J.; Kruss, S. Quantum Defects in Fluorescent Carbon Nanotubes for Sensing and Mechanistic Studies. *The Journal of Physical Chemistry C* **2021**, *125* (33), 18341–18351. https://doi.org/10.1021/acs.jpcc.1c05432.

(38) Kim, M.; Chen, C.; Wang, P.; Mulvey, J. J.; Yang, Y.; Wun, C.; Antman-Passig, M.; Luo, H.-B.; Cho, S.; Long-Roche, K.; Ramanathan, L. V.; Jagota, A.; Zheng, M.; Wang, Y.; Heller, D. A. Detection of Ovarian Cancer via the Spectral Fingerprinting of Quantum-Defect-Modified Carbon Nanotubes in Serum by Machine Learning. *Nat Biomed Eng* **2022**, *6* (3), 267–275. https://doi.org/10.1038/s41551-022-00860-y.

(39) He, X.; Htoon, H.; Doorn, S. K.; Pernice, W. H. P.; Pyatkov, F.; Krupke, R.; Jeantet, A.; Chassagneux, Y.; Voisin, C. Carbon Nanotubes as Emerging Quantum-Light Sources. *Nat Mater* **2018**, *17* (8), 663–670. https://doi.org/10.1038/s41563-018-0109-2.

(40) Zorn, N. F.; Berger, F. J.; Zaumseil, J. Charge Transport in and Electroluminescence from Sp^3-Functionalized Carbon Nanotube Networks. *ACS Nano* **2021**, *15* (6), 10451–10463. https://doi.org/10.1021/acsnano.1c02878.

(41) Sebastian, F. L.; Zorn, N. F.; Settele, S.; Lindenthal, S.; Berger, F. J.; Bendel, C.; Li, H.; Flavel, B. S.; Zaumseil, J. Absolute Quantification of Sp^3 Defects in Semiconducting Single-Wall Carbon Nanotubes by Raman Spectroscopy. *J Phys Chem Lett* **2022**, *13* (16), 3542–3548. https://doi.org/10.1021/acs.jpclett.2c00758.

(42) Sanchez-Valencia, J. R.; Dienel, T.; Gröning, O.; Shorubalko, I.; Mueller, A.; Jansen, M.; Amsharov, K.; Ruffieux, P.; Fasel, R. Controlled Synthesis of Single-Chirality Carbon Nanotubes. *Nature* **2014**, *512* (7512), 61–64. https://doi.org/10.1038/nature13607.

(43) Liu, B.; Wu, F.; Gui, H.; Zheng, M.; Zhou, C. Chirality-Controlled Synthesis and Applications of Single-Wall Carbon Nanotubes. *ACS Nano* **2017**, *11* (1), 31–53. https://doi.org/10.1021/acsnano.6b06900.

(44) Nißler, R.; Kurth, L.; Li, H.; Spreinat, A.; Kuhlemann, I.; Flavel, B. S.; Kruss, S. Sensing with Chirality-Pure Near-Infrared Fluorescent Carbon Nanotubes. *Anal Chem* **2021**, *93* (16), 6446–6455. https://doi.org/10.1021/acs.analchem.1c00168.

(45) Nißler, R.; Ackermann, J.; Ma, C.; Kruss, S. Prospects of Fluorescent Single-Chirality Carbon Nanotube-Based Biosensors. *Anal Chem* **2022**, *94* (28), 9941–9951. https://doi.org/10.1021/acs.analchem.2c01321.

(46) Arnold, M. S.; Stupp, S. I.; Hersam, M. C. Enrichment of Single-Walled Carbon Nanotubes by Diameter in Density Gradients. *Nano Lett* **2005**, *5* (4), 713–718. https://doi.org/10.1021/nl050133o.

(47) Zheng, M.; Semke, E. D. Enrichment of Single Chirality Carbon Nanotubes. *J Am Chem Soc* **2007**, *129* (19), 6084–6085. https://doi.org/10.1021/ja071577k.

(48) Huang, X.; Mclean, R. S.; Zheng, M. High-Resolution Length Sorting and Purification of DNA-Wrapped Carbon Nanotubes by Size-Exclusion Chromatography. *Anal Chem* **2005**, *77* (19), 6225–6228. https://doi.org/10.1021/ac0508954.

(49) Moore, K. E.; Pfohl, M.; Hennrich, F.; Chakradhanula, V. S. K.; Kuebel, C.; Kappes, M. M.; Shapter, J. G.; Krupke, R.; Flavel, B. S. Separation of Double-Walled Carbon Nanotubes by Size Exclusion Column Chromatography. *ACS Nano* **2014**, *8* (7), 6756–6764. https://doi.org/10.1021/nn500756a.

(50) Arnold, M. S.; Green, A. A.; Hulvat, J. F.; Stupp, S. I.; Hersam, M. C. Sorting Carbon Nanotubes by Electronic Structure Using Density Differentiation. *Nat Nanotechnol* **2006**, *1* (1), 60–65. https://doi.org/10.1038/nnano.2006.52.

(51) Yang, F.; Wang, M.; Zhang, D.; Yang, J.; Zheng, M.; Li, Y. Chirality Pure Carbon Nanotubes: Growth, Sorting, and Characterization. *Chem Rev* **2020**, *120* (5), 2693–2758. https://doi.org/10.1021/acs.chemrev.9b00835.

(52) Li, H.; Gordeev, G.; Garrity, O.; Peyyety, N. A.; Selvasundaram, P. B.; Dehm, S.; Krupke, R.; Cambré, S.; Wenseleers, W.; Reich, S.; Zheng, M.; Fagan, J. A.; Flavel, B. S. Separation of Specific Single-Enantiomer Single-Wall Carbon Nanotubes in the Large-Diameter Regime. *ACS Nano* **2020**, *14* (1), 948–963. https://doi.org/10.1021/acsnano.9b08244.

(53) Li, H.; Sims, C. M.; Kang, R.; Biedermann, F.; Fagan, J. A.; Flavel, B. S. Isolation of the (6,5) Single-Wall Carbon Nanotube Enantiomers by Surfactant-Assisted Aqueous Two-Phase Extraction. *Carbon N Y* **2023**, *204*, 475–483. https://doi.org/10.1016/j.carbon.2022.12.071.

(54) Zheng, M.; Jagota, A.; Strano, M. S.; Santos, A. P.; Barone, P.; Chou, S. G.; Diner, B. A.; Dresselhaus, M. S.; Mclean, R. S.; Onoa, G. B.; Samsonidze, G. G.; Semke, E. D.; Usrey, M.; Walls, D. J. Structure-Based Carbon Nanotube Sorting by Sequence-Dependent DNA Assembly. *Science (1979)* **2003**, *302* (5650), 1545–1548. https://doi.org/10.1126/science.1091911.

(55) Ghosh, S.; Bachilo, S. M.; Weisman, R. B. Advanced Sorting of Single-Walled Carbon Nanotubes by

Nonlinear Density-Gradient Ultracentrifugation. *Nat Nanotechnol* **2010**, *5* (6), 443–450. https://doi.org/10.1038/nnano.2010.68.

(56) Fleurier, R.; Lauret, J.-S.; Lopez, U.; Loiseau, A. Transmission Electron Microscopy and UV-Vis-IR Spectroscopy Analysis of the Diameter Sorting of Carbon Nanotubes by Gradient Density Ultracentrifugation. *Adv Funct Mater* **2009**, *19* (14), 2219–2223. https://doi.org/10.1002/adfm.200801778.

(57) Nish, A.; Hwang, J.-Y.; Doig, J.; Nicholas, R. J. Highly Selective Dispersion of Single-Walled Carbon Nanotubes Using Aromatic Polymers. *Nat Nanotechnol* **2007**, *2* (10), 640–646. https://doi.org/10.1038/nnano.2007.290.

(58) Tange, M.; Okazaki, T.; Iijima, S. Selective Extraction of Large-Diameter Single-Wall Carbon Nanotubes with Specific Chiral Indices by Poly(9,9-Dioctylfluorene- *Alt* -Benzothiadiazole). *J Am Chem Soc* **2011**, *133* (31), 11908–11911. https://doi.org/10.1021/ja204698d.

(59) Tanaka, T.; Urabe, Y.; Hirakawa, T.; Kataura, H. Simultaneous Chirality and Enantiomer Separation of Metallic Single-Wall Carbon Nanotubes by Gel Column Chromatography. *Anal Chem* **2015**, *87* (18), 9467–9472. https://doi.org/10.1021/acs.analchem.5b02563.

(60) Liu, H.; Nishide, D.; Tanaka, T.; Kataura, H. Large-Scale Single-Chirality Separation of Single-Wall Carbon Nanotubes by Simple Gel Chromatography. *Nat Commun* **2011**, *2* (1), 309. https://doi.org/10.1038/ncomms1313.

(61) Flavel, B. S.; Moore, K. E.; Pfohl, M.; Kappes, M. M.; Hennrich, F. Separation of Single-Walled Carbon Nanotubes with a Gel Permeation Chromatography System. *ACS Nano* **2014**, *8* (2), 1817–1826. https://doi.org/10.1021/nn4062116.

(62) Lyu, M.; Meany, B.; Yang, J.; Li, Y.; Zheng, M. Toward Complete Resolution of DNA/Carbon Nanotube Hybrids by Aqueous Two-Phase Systems. *J Am Chem Soc* **2019**, *141* (51), 20177–20186. https://doi.org/10.1021/jacs.9b09953.

(63) Li, H.; Gordeev, G.; Garrity, O.; Reich, S.; Flavel, B. S. Separation of Small-Diameter Single-Walled Carbon Nanotubes in One to Three Steps with Aqueous Two-Phase Extraction. *ACS Nano* **2019**, *13* (2), 2567–2578. https://doi.org/10.1021/acsnano.8b09579.

(64) Fagan, J. A.; Khripin, C. Y.; Silvera Batista, C. A.; Simpson, J. R.; Hároz, E. H.; Hight Walker, A. R.; Zheng, M. Isolation of Specific Small-Diameter Single-Wall Carbon Nanotube Species via Aqueous Two-Phase Extraction. *Advanced Materials* **2014**, *26* (18), 2800–2804. https://doi.org/10.1002/adma.201304873.

(65) Ao, G.; Khripin, C. Y.; Zheng, M. DNA-Controlled Partition of Carbon Nanotubes in Polymer Aqueous Two-Phase Systems. *J Am Chem Soc* **2014**, *136* (29), 10383–10392. https://doi.org/10.1021/ja504078b.

(66) Li, H.; Sims, C. M.; Kang, R.; Biedermann, F.; Fagan, J. A.; Flavel, B. S. Isolation of the (6,5) Single-Wall Carbon Nanotube Enantiomers by Surfactant-Assisted Aqueous Two-Phase Extraction. *Carbon* **2023**, *204*, 475–483. https://doi.org/10.1016/j.carbon.2022.12.071.

(67) Fagan, J. A. Aqueous Two-Polymer Phase Extraction of Single-Wall Carbon Nanotubes Using Surfactants. *Nanoscale Adv* **2019**, *1* (9), 3307–3324. https://doi.org/10.1039/C9NA00280D.

(68) Langenbacher, R.; Budhathoki-Uprety, J.; Jena, P. v.; Roxbury, D.; Streit, J.; Zheng, M.; Heller, D. A. Single-Chirality Near-Infrared Carbon Nanotube Sub-Cellular Imaging and FRET Probes. *Nano Lett* **2021**, *21* (15), 6441–6448. https://doi.org/10.1021/acs.nanolett.1c01093.

(69) Cognet, L.; Tsyboulski, D. A.; Rocha, J.-D. R.; Doyle, C. D.; Tour, J. M.; Weisman, R. B. Stepwise Quenching of Exciton Fluorescence in Carbon Nanotubes by Single-Molecule Reactions. *Science (1979)* **2007**, *316* (5830), 1465–1468. https://doi.org/10.1126/science.1141316.

(70) Subbaiyan, N. K.; Cambré, S.; Parra-Vasquez, A. N. G.; Hároz, E. H.; Doorn, S. K.; Duque, J. G. Role of Surfactants and Salt in Aqueous Two-Phase Separation of Carbon Nanotubes toward Simple Chirality Isolation. *ACS Nano* **2014**, *8* (2), 1619–1628. https://doi.org/10.1021/nn405934y.

(71) Wang, P.; Fortner, J.; Luo, H.; Kłos, J.; Wu, X.; Qu, H.; Chen, F.; Li, Y.; Wang, Y. H. Quantum Defects: What Pairs with the Aryl Group When Bonding to the Sp2Carbon Lattice of Single-Wall Carbon Nanotubes? *J Am Chem Soc* **2022**, *144* (29), 13234–13241. https://doi.org/10.1021/jacs.2c03846.

(72) Paulus, G. L. C.; Wang, Q. H.; Strano, M. S. Covalent Electron Transfer Chemistry of Graphene with Diazonium Salts. *Acc Chem Res* **2013**, *46* (1), 160–170. https://doi.org/10.1021/ar300119z.

(73) Usrey, M. L.; Lippmann, E. S.; Strano, M. S. Evidence for a Two-Step Mechanism in Electronically Selective Single-Walled Carbon Nanotube Reactions. *J Am Chem Soc* **2005**, *127* (46), 16129–16135. https://doi.org/10.1021/ja0537530.

(74) Powell, L. R.; Piao, Y.; Wang, Y. Optical Excitation of Carbon Nanotubes Drives Localized Diazonium Reactions. *J Phys Chem Lett* **2016**, *7* (18), 3690–3694. https://doi.org/10.1021/acs.jpclett.6b01771.

(75) Zhang, J.; Boghossian, A. A.; Barone, P. W.; Rwei, A.; Kim, J.-H.; Lin, D.; Heller, D. A.; Hilmer, A. J.; Nair, N.; Reuel, N. F.; Strano, M. S. Single Molecule Detection of Nitric Oxide Enabled by d(AT) $_{15}$ DNA Adsorbed to Near Infrared Fluorescent Single-Walled Carbon Nanotubes. *J Am Chem Soc* **2011**, *133* (3), 567–581. https://doi.org/10.1021/ja1084942.

(76) Hartmann, N. F.; Yalcin, S. E.; Adamska, L.; Hároz, E. H.; Ma, X.; Tretiak, S.; Htoon, H.; Doorn, S. K. Photoluminescence Imaging of Solitary Dopant Sites in Covalently Doped Single-Wall Carbon Nanotubes. *Nanoscale* **2015**, *7* (48), 20521–20530. https://doi.org/10.1039/C5NR06343D.

(77) Hertel, T.; Himmelein, S.; Ackermann, T.; Stich, D.; Crochet, J. Diffusion Limited Photoluminescence Quantum Yields in 1-D Semiconductors: Single-Wall Carbon Nanotubes. *ACS Nano* **2010**, *4* (12), 7161–7168. https://doi.org/10.1021/nn101612b.

(78) Danné, N.; Kim, M.; Godin, A. G.; Kwon, H.; Gao, Z.; Wu, X.; Hartmann, N. F.; Doorn, S. K.; Lounis, B.; Wang, Y.; Cognet, L. Ultrashort Carbon Nanotubes That Fluoresce Brightly in the Near-Infrared. *ACS Nano* **2018**, *12* (6), 6059–6065. https://doi.org/10.1021/acsnano.8b02307.

(79) Rossi, J. E.; Soule, K. J.; Cleveland, E.; Schmucker, S. W.; Cress, C. D.; Cox, N. D.; Merrill, A.; Landi, B. J. Removal of Sodium Dodecyl Sulfate Surfactant from Aqueous Dispersions of Single-Wall Carbon Nanotubes. *J Colloid Interface Sci* **2017**, *495*, 140–148. https://doi.org/10.1016/j.jcis.2017.01.117.

(80) Streit, J. K.; Bachilo, S. M.; Ghosh, S.; Lin, C.-W.; Weisman, R. B. Directly Measured Optical Absorption Cross Sections for Structure-Selected Single-Walled Carbon Nanotubes. *Nano Lett* **2014**, *14* (3), 1530–1536. https://doi.org/10.1021/nl404791y.

(81) Schöppler, F.; Mann, C.; Hain, T. C.; Neubauer, F. M.; Privitera, G.; Bonaccorso, F.; Chu, D.; Ferrari, A. C.; Hertel, T. Molar Extinction Coefficient of Single-Wall Carbon Nanotubes. *The Journal of Physical Chemistry C* **2011**, *115* (30), 14682–14686. https://doi.org/10.1021/jp205289h.

(82) Boghossian, A. A.; Zhang, J.; Le Floch-Yin, F. T.; Ulissi, Z. W.; Bojo, P.; Han, J.-H.; Kim, J.-H.; Arkalgud, J. R.; Reuel, N. F.; Braatz, R. D.; Strano, M. S. The Chemical Dynamics of Nanosensors Capable of Single-Molecule Detection. *J Chem Phys* **2011**, *135* (8), 084124. https://doi.org/10.1063/1.3606496.

TOC GRAPHIC

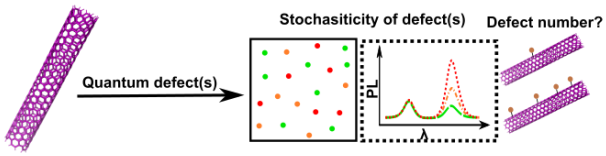
Stochasitiicity of defect(s)
Defect number?
Quantum defect(s)
PL
λ